Mode profiling of semiconductor nanowire lasers

Dhruv Saxena[*], *Fan Wang*[†], *Qian Gao, Sudha Mokkapati, Hark Hoe Tan, Chennupati Jagadish*

Department of Electronic Materials Engineering, Research School of Physics and Engineering, The Australian National University, Canberra, A.C.T. 2601, Australia.

KEYWORDS: nanowire lasers, semiconductor nanowires, mode characterization, far-field characterization, Fourier space imaging

ABSTRACT: We experimentally determine the lasing mode(s) in optically pumped semiconductor nanowire lasers. The spatially resolved and angle-resolved far-field emission profiles of single InP nanowire lasers lying horizontally on a SiO_2 substrate are characterized in a micro-photoluminescence (μ-PL) setup. The experimentally obtained polarization dependent far-field profiles match very well with numerical simulations and enable unambiguous identification of the lasing mode(s). This technique can be applied to characterize lasing modes in other type of nanolasers that are integrated on a substrate, in either vertical or horizontal configurations.

MAIN TEXT: Semiconductor nanowires enable the integration of efficient light emitters with a waveguide or a cavity, and so have been widely used for the development of novel coherent light sources at the nanoscale, such as single photon emitters[1, 2] and nanolasers[3-10], which are essential

components for future nanophotonic integrated systems. The large index contrast between the nanowire and its surrounding environment and the subwavelength size of their cross-section gives rise to unique optical properties, such as strong waveguiding[11] and strong reflection/scattering at nanowire end facets[12], which are advantageous for reducing the threshold requirement and for downscaling the physical volume of photonic lasers[13]. Several different nanowire lasers, in a wide range of material systems, that are integrated on a substrate, in either vertical or horizontal configurations, have been demonstrated. Majority of these demonstrations have used nanowires lying on low index substrates with their end facts exposed to air, to maximize the index contrast and thus realize low thresholds. In this configuration, emission from the nanowire laser can also be easily coupled to photonic[14, 15] or plasmonic[16] waveguides, which is an important consideration for integrating these devices in nanophotonic circuits.

The far-field emission from nanowire lasers, and in general all nanoscale lasers, is not collimated due to their small dimensions and fully vectorial nature of the cavity modes[13]. The far-field emission pattern is further complicated by scattering of the propagating modes at the nanowire end facets. A theoretical study on free-standing nanowires showed that the directionality of the far-field emission from the nanowire end-facet depends on the propagating mode and the nanowire diameter[17]. The polarization of the far-field emission also depends on the mode type. In order to integrate nanowire lasers with other optical components, such as waveguides, the polarization and directionality of the lasing mode needs to be understood theoretically and characterized experimentally. However for nanowire lasers that are lying on a substrate, the substrate imposes difficulties for both theoretical analysis and experimental characterization of the far-field emission. Most previous studies have avoided these complications, by suspending the nanowire in air, and performing 'head-on' measurements[18, 19]. While this method enables characterization of lasing

modes, it requires careful alignment of the nanowire with respect to the edge of the substrate and may not be suitable to characterize emission from lasing modes whose angular emission pattern lies outside the collection angle of the limited numerical aperture objective lens. Very recently, angle-resolved spectral mapping was used to characterize the axial order of cavity modes supported in nanowires lying on a substrate.[20] However this technique only provides a 1D map of the far-field emission pattern, which may be insufficient to uniquely characterize the lasing mode.

Here we present a simple imaging technique to characterize the lasing mode(s) in nanowire lasers that are lying horizontally on a substrate, which does not require them to be positioned in an idealized configuration, such as being suspended in air. Our approach is based on profiling the far-field intensity pattern of nanowire lasers. The polarization and directionality of the emission is characterized by resolving the transverse component of the wave-vector on the Fourier plane. This technique has been used recently to study the polarization and directionality of spontaneous emission from vertically standing nanowires[21-23] and characterize modes in photonic crystal microcavities[24]. In this study we deliberately design nanowire lasers to lase from different guided modes and then characterize their far-field profiles to validate the technique. The polarization and angular distribution of intensity of emission intensity in the far-field is distinct for each of the lasing modes characterized and match very well with numerical simulations. The mode profiling thus enables the lasing mode(s) in nanowire lasers to be unambiguously identified.

We model the threshold gain for a horizontally lying nanowire laser, in order to design nanowire lasers that would lase from different waveguide modes. The threshold condition for laser oscillation is given by equating the round-trip modal gain with the round-trip losses[25]. For nanowire lasers behaving as Fabry-Perot type cavities, the predominant losses occur at the end

facets[18] (mirror losses) and so the threshold gain can be modelled using $\Gamma g_{th} \sim \frac{1}{L} \ln\left(\frac{1}{R}\right)$, where Γ is the mode confinement factor, g_{th} is the threshold gain, L is the cavity length and R is the geometric mean of the mode reflectances at the end facets. We use this equation to model the threshold gain for an InP nanowire lying on a SiO_2 substrate. Figure 1 shows the threshold gain as a function of the nanowire diameter, for the various guided modes supported in this diameter range. The nanowire is modelled as a regular hexagonal prism with L=5 μm, and the diameter here refers to the widest length of the nanowire cross-section, as shown in the inset of Figure 1. For these calculations, numerical methods were used to calculate Γ and R as a function of the nanowire diameter for the different guided modes supported (see Supporting Information).

In Figure 1, the diameter at which the threshold gain is minimized is different for each mode. For example, the $HE11_b$, TE01 and TM01 modes have a minimum threshold gain of 1580, 610 and 550 cm^{-1} for nanowire with a diameter of 270, 380 and 500 nm, respectively. Overall, for the range of diameters considered in the modelling, the threshold gain is lowest for the TM01 mode, for nanowire with a diameter of 500 nm. In general, the threshold gain reduces with increasing nanowire diameter, as a result of improved mode overlap with the gain medium and larger facet reflectivity (see Supporting Information). Since the mode with the lowest threshold gain is the most favored mode to lase[26], the threshold gain modelling presented in Figure 1 enables us to design nanowire lasers that would lase from a particular guided mode. For example, for nanowires with diameters in the range 220-270 nm, the $HE11_b$ mode has the lowest threshold gain requirement and so is likely to lase, whereas for nanowire diameters in the ranges 270-450 nm and 450-500 nm, the TE01 and TM01 modes have the lowest threshold gain requirement and are likely to lase, respectively. We use these calculations to design nanowire lasers that would lase from $HE11_b$, TE01 and TM01 modes.

InP nanowires with three different diameters were grown using selective-area metal organic vapor phase epitaxy on patterned InP substrates (see Methods). The nanowire diameters were 250±2 nm, 330±5 nm, and 480±20 nm for the three samples, as measured from scanning electron microscope (SEM) images (see Supporting Information). The diameter of the nanowires was controlled by varying the mask pattern (diameter of etched hole and pitch of the array) and both the diameter and length of the nanowires was controlled by varying the growth parameters. The growth parameters were adopted from Ref. 10, which enable the growth of stacking fault-free pure wurtzite phase InP nanowires, with high quantum efficiencies. The InP nanowires grown for this study are expected to be of similar quality. Furthermore, the nanowires are structurally uniform; they have a perfect crystallographic flat top end facet and smooth un-tapered side walls (see Supporting Information). The flat top end facet functions as a low-loss dielectric mirror for waveguide modes supported along the nanowire axis and the smooth un-tapered side walls ensure modes are uniformly guided, without change in confinement and without scattering losses, along the nanowire. Thus, the high material and structural quality of these nanowires makes them suitable as low-threshold lasers and their diameters are appropriate for characterizing lasing from different waveguide modes, namely $HE11_b$, TE01 and TM01 modes.

The as-grown nanowires were transferred onto SiO_2 substrates for optical measurements. Individual InP nanowires were optically pumped at low-temperature (6 K) in a micro-photoluminescence (μ-PL) setup (see Methods) and the PL spectrum was measured at various pump intensities. The integrated spectral emission, which is proportional to the output power from the nanowire, as a function of pump intensity was analyzed for three different nanowires, of dimensions: (I) d=250 nm, L=3.9 μm, (II) d=330 nm, L=2.8 μm and (III) d=460 nm, L=8.1 μm (see Supporting Information). The variation of the output power with pump intensity for the three

different nanowires is shown in Figure 2. The log-log plot of these datasets show a nonlinear 'S' like response, which is the typical threshold behavior of lasers[26, 27]. Overlaid on the datasets are curves calculated from an analytical model for the total output intensity of a laser[27], with different values of the parameter x_0. This parameter is a dimensionless measure of the spontaneous emission rate; it is proportional to the spontaneous emission factor β and related to the value $1/p$, where p is the number of resonant cavity modes that can be coupled to within the emission linewidth[26]. The values x_0 =: (I) 0.22, (II) 0.06, (III) 0.018, provide a good fit to the experimental data for the three different diameter nanowires, respectively. The 'S' like curves describe the transition from spontaneous emission (linear regime below threshold) to lasing (linear regime above threshold) via amplified spontaneous emission (ASE) (super-linear regime). The sharpness of this transition at threshold depends on the value of x_0, or equivalently $1/p$, and becomes less distinct as x_0 increases, or as p reduces. In Figure 1, the sharpness of the transition at threshold is observed to be strongly dependent on the nanowire diameter – the gradient at threshold becomes less sharp and distinct with reducing diameter. The larger value of x_0, or β factor, observed for smaller diameter nanowire lasers is a direct consequence of the reduction in p.

The lasing spectra just above threshold ($P = 1.2*P_{th}$) from the three different diameter nanowire lasers are shown in the inset of Figure 2. A dominant lasing peak is observed at this pump intensity for each of the nanowire lasers. This lasing peak corresponds to a single axial mode of the Fabry-Perot type cavity. The other peaks observed in the spectra are due to amplification of other axial or transverse modes supported in the cavity. The lasing peaks at 800 nm, 830 nm and 840 nm from nanowire lasers I-III have a full width at half maximum (FWHM) of 4.5, 3, 1.5 nm, respectively. The lasing peak at 800 nm is composed of two closely spaced peaks, at 799.5 nm and 802 nm (see Supporting Information). The spectral position of these two peaks corresponds to the respective

wavelength of $HE11_b$ and $HE11_a$ modes of axial order 24 in this nanowire (see Supporting Information). The intensity of the peak at 799.5 nm is about twice as large as the intensity of the peak at 802 nm, which suggests that the $HE11_b$ mode is the dominant lasing mode in this nanowire. This is also consistent with our threshold gain modelling predictions. We note here that other transverse modes, other than the mode with the lowest threshold gain, can lase if their threshold gain requirements are close to the lowest threshold gain value. In an ideal laser, operating under steady-state conditions, multiple transverse modes can lase if the difference in losses between the most preferred lasing mode and other modes is of the order $1/\sqrt{p}$ or smaller[26], where p was defined previously. We have calculated the range of values above the minimum threshold gain value for which the difference in losses are less than $1/\sqrt{p}$ (see Supporting Information), shown in the grey region in Figure 1. Modes that have threshold gain requirements in this region are likely to lase. The threshold gain requirement for the $HE11_a$ mode is within this grey region, which is possibly the reason we observe multimode behavior from nanowire laser I.

The nanowire lasers I-III characterized in Figure 2, based on their dimensions, are expected to lase from different guided modes. To experimentally characterize the lasing mode, we profile the far-field emission from these nanowire lasers. We do this at a pump power just above threshold, where the emission spectrum is dominated by a single lasing peak, corresponding to the designed lasing mode. Operating close to the lasing threshold prevents the nanowires to lase from other possible axial and transverse modes. The possible drift in threshold due to heating is mitigated by performing these measurements at low temperature. In the next sections we discuss the mode profiling of the nanowire lasers I-III and characterization of the different lasing modes.

The spatial intensity profile of laser emission from the three different nanowire lasers was obtained using the same setup as to collect the spectra, by using the 0^{th} order of the grating and the spectrometer CCD (see Methods). A linear polarizer in front of the spectrometer was used to resolve the emission pattern under two different orientations, parallel and perpendicular to the nanowire axis. Figure 3 shows the focal plane images of the three different nanowire lasers under the two different orientations of the analyzer, at pump power just above threshold. In these images the pump laser has been filtered out, and the color bar axes are on a log scale. Intense emission is observed from the nanowire end facets, which indicates that the nanowires behave as Fabry-Perot type cavities. The spatial pattern of the emission from the end facets is polarization dependent and is different for each of three nanowire lasers. Furthermore, the degree of linear polarization is different for each of the three nanowire lasers; the polarization ratio, $\rho = (I_{\parallel} - I_{\perp})/(I_{\parallel} + I_{\perp})$, measured for the emission above threshold from the three different nanowires is I) -0.06, II) -0.34 and III) 0.33. This suggests that each of the three nanowire lasers lase from different transverse (or waveguide) modes. To investigate this, we performed FDTD simulations to determine the electric field intensity profiles in the near-field of the nanowire for different waveguide modes (see Supporting Information). The measured dimensions of the nanowire lasers were used for the nanowire dimensions in these simulations, and the nanowires were modelled with perfect end facets, although one end facet of the nanowire is rough due to uneven breaking during the transfer process (see Supporting Information). The surface roughness of the end facet results in greater scattering and distorts the mode profile, which is evident in the images shown in Figure 3b-c (the rough end corresponds to the bottom end in these images).

The polarization resolved electric field intensity profiles in the near-field of the nanowire for the different waveguide modes is shown in Supporting Information. Since the optical modes in the

nanowire are fully vectorial[13], all three electric field components are non-zero. The polarization resolved near-field profiles parallel and perpendicular to the nanowire axis for the $HE11_b$, TE01, TM01 modes (see Supporting Information) correlate qualitatively with the experimentally obtained far-field profiles shown in Figure 3a-c, respectively. The differences between the experimental and simulated profiles are because; in the experiment, the polarization analysis is performed on the far-fields, in the parallel light path behind the infinity corrected objective lens, and in simulations, we resolve fields in the near-field of the nanowire laser. Though the polarization resolved far-field mode profiles can be calculated from the simulation data by further analysis, the simulated near-field spatial profiles already provide a qualitative basis to distinguish different lasing modes and suggest that the nanowire lasers of diameters 250 nm, 330 nm, 460 nm, lase from $HE11_b$, TE01, TM01 modes, respectively, which is also consistent with the threshold gain predictions from Figure 1.

The polarization dependent focal plane images shown in Figure 3 demonstrate a simple method to profile different lasing modes in nanowire lasers. However, these intensity profiles do not provide information on the directionality of emission. Experimental characterization of the directionality of the laser emission is required for appropriate integration of these devices with other optical components. The directionality of the far-fields can be experimentally characterized by imaging the back focal plane (BFP), or Fourier plane, of the objective lens, since on this plane the far-fields are resolved in angular coordinates[28]. In our μ-PL setup, we placed an additional imaging lens (f=250 mm) and a CCD camera to image the BFP. The lens was placed at a distance 2f from the BFP, and the CCD camera was placed at a distance 2f from the lens, in order to have 1:1 correspondence between the image planes. A filter was also used to filter out the emission from the pump laser.

The BFP images of the three nanowire lasers of diameters 250 nm, 330 nm, 460 nm, at pump intensity just above threshold are shown in the left hand panel of Figures 4a-c, respectively. The angular coordinates are overlaid on these images, where θ corresponds to the solid angle of emission and ϕ corresponds to the azimuthal angle of emission. The nanowires are orientated horizontally (ϕ=0°, or 180°) in these images. Distinct interference fringes that are perpendicular to the nanowire axis are observed above threshold. These interference fringes are due to spatially coherent emission from the nanowire end facets, and are analogous to the interference fringes observed when two slits are illuminated by a spatially coherent source, as in Young's double slit experiment[29]. The spacing of these fringes across the BFP depends upon the nanowire length (L) and the emission wavelength (λ). The position offset of these fringes with respect to the center of the BFP depends on the phase difference between the emission from the nanowire ends[20, 30], which in turn depends on the axial order, or parity, of the lasing mode(s)[20], and the mode type (see Supporting Information). The visibility of the interference pattern depends on the degree of first order coherence of the emission and the spectral purity (strong and narrow emission at a single frequency). Well below threshold, due to spectrally broad and incoherent spontaneous emission, no interference fringes are observed across the BFP. The visibility of the interference fringes increases by either increasing the material gain, in order to amplify the spatially coherent emission above the strong spontaneous emission background, or by spectrally resolving the emission[20]. The line plots below the BFP images, in the left hand panel of Figures 4a-c, show the intensity along the line ϕ=0° or 180° of the BFP, which corresponds to the plane aligned with the nanowire axis. Sinusoidal variation in the intensity as a function of angle is evident in all line plots. The irregular peak at θ=8° and θ=0° in the line plots of Figures 4a and b, respectively, are due to the strong back reflection of the pump laser from the substrate, which was not adequately filtered out by the filters.

These irregular peaks suggest that the sample in Figure 4a was slightly inclined (at an angle 8°) with respect to the optical axis of the objective lens during measurements, whereas the sample in Figure 4b was perpendicular to the optical axis of the objective lens.

The intensity fringes observed in BFP enable the length of the nanowire to be easily determined. Overlaid on the line plots of the data in Figures 4a-c are fits obtained from a simple model for the nanowire laser far-field emission pattern (see Supporting Information). In this model the nanowire ends are modelled as two point sources that are a distance L apart, where L is the nanowire length. The wavelength of the emission is taken from the spectral measurements of the nanowire lasers (inset of Figure 2) and the phase difference is chosen to fit the data (see Supporting Information for parameter values). The fits to the data shown in the line plots in Figures 4a-c, give estimates of L of 3.5, 2.81, 8.14 μm, respectively, which are consistent with the measured length of the nanowires from SEM images.

The fits obtained from our simple analytical model explain the spacing of the interference fringes. In the left hand panel of Figures 4a-c, we observe that the intensity of the interference fringes is modulated across the BFP and the intensity variation is different for each of the nanowire lasers characterized. This is because the angle-resolved far-field emission patterns of the nanowire lasers are a product of the interference pattern resulting from the spatially coherent emission from nanowire ends and the far-field emission pattern of the different lasing modes. To verify this, we placed a linear polarizer in front of the CCD camera to resolve the emission patterns under two orthogonal directions, parallel and perpendicular to the nanowire. The experimentally obtained BFP images for the three different nanowire lasers under different orientations of the polarizer are shown in right hand panels of Figures 4a-c. The direction of the polarization axis is indicated by the white arrow on the top right hand corner of these images. Interference fringes are observed in

all these polarization resolved images, but they are clearly modulated in intensity across the BFP. The polarization resolved far-field intensity patterns are distinct and unique for all the three different samples studied, and indicate that it may be possible to unambiguously identify the lasing modes based on these distinct far-field patterns.

We have performed FDTD simulations to calculate the angle-resolved far-field pattern for different guided modes, in a nanowire laser that is lying horizontally on a substrate (see Supporting Information). The measured dimensions of the nanowire lasers from SEM images were used for the nanowire dimensions in these simulations, and the mode wavelength was taken from spectral measurements (inset of Figure 2). The far-field is calculated for the emission into air, in the upper hemisphere perpendicular to the substrate, for solid angles less than 44.4°, which corresponds to a numerical aperture (NA) of 0.7 used in experiments. The simulated far-field patterns for $HE11_{(a,b)}$, TE01 and TM01 modes are shown in Figures 4d-f, respectively, where the total electric field intensity is shown on the left hand panel and the polarization resolved field intensity patterns, parallel and perpendicular to the nanowire axis, are shown on the right hand panel. The polarization resolved intensity patterns shown here have been corrected for the phase shift due to transmission through the sapphire window, which was used in the cryostat in our low-temperature μ-PL measurements (see Supporting Information). The phase shift due to the birefringence of the sapphire window results in significant modification of the polarization of the far-fields and is the main reason for the low polarization anisotropy of the lasing emission observed in our experiments. The polarization ratio, ρ, calculated by integrating the simulated far-fields across the BFP, in Figures 4d-f, is -0.09, -0.37 and 0.41, respectively. These values are consistent with the polarization ratios calculated for the three different nanowire lasers from experiments. The un-

corrected polarization resolved mode far-field intensity patterns and their polarization ratios are provided in the Supporting Information.

The system corrected far-field patterns of different guided modes in Figures 4d-f correlate well with our experimental results and enable us to unambiguously identify the lasing modes in nanowire lasers I-III. In Figure 4d, the simulated far-field patterns shown are a superposition of the far-field patterns of both $HE11_a$ and $HE11_b$ modes. The mode wavelength was 800 nm in these simulations, corresponding to the dominant peak observed at λ~800 nm in the spectra for nanowire laser I (see inset of Figure 2). There other peaks in the spectra corresponding to different axial modes and the tilt of the sample with respect to the optical axis were not modelled in the simulations. We find that the simulated far-field patterns only match our experimental data when we superimpose far-field patterns for both $HE11_a$ and $HE11_b$ modes, with the intensity ratio of 1:3, respectively. Any other combinations of the relative intensity of the modes do not match with our experimental data. This suggests that both HE11 modes are observed in the emission from nanowire laser I, but the emission is dominated by $HE11_b$ mode, since it has a lower threshold gain requirement (see Figure 1). For nanowire lasers II and III, the system corrected far-field patterns for TE01 and TM01 modes in Figures 4e-f correlate well with the experimental data shown in Figures 4b-c, respectively. Thus nanowire lasers II and III lase from TE01 and TM01 modes, respectively.

In this study we have used the Fourier plane imaging technique to characterize the lasing modes in semiconductor nanowire lasers. This characterization technique is straightforward to implement in standard μ-PL system and does not require nanowire lasers to be free-standing or suspended off from the substrate. Since this technique is applicable to nanowire lasers that are lying on a substrate, it can be used for characterizing nanowire lasers and LEDs that have been integrated

with other optical components, such as waveguides and gratings[14, 31-33]. Moreover, it enables the directionality and polarization of the far-fields to be measured experimentally, which will aid the design of integrated components for better out-coupling of light and/or collimating light from nanowire lasers. In general, our approach can be applied to characterize ASE/lasing modes in other types of nanolasers[34-36], which are also integrated on a substrate in either horizontal or vertical configurations. For nanolasers that behave as Fabry-Perot like cavities, this characterization technique enables an alternative way to determine the cavity length, without relying on SEM characterization methods, which can have degrading effects on the performance of the device due to electron beam damage.

Methods

Nanowire growth. InP nanowires were grown on patterned (111)A InP substrates using selective-area metal organic vapor phase epitaxy (SA-MOVPE). For patterning the substrates, 30 nm SiO_2 mask layer was first deposited on the substrates and then electron beam lithography (EBL) was used to write a pattern consisting of hexagonal arrays of circles. The pattern was then transferred to the SiO_2 mask by etching using buffered hydrogen fluoride (BHF) solution. A trim etching step using phosphoric acid solution was used to remove a thin layer of the exposed InP within the holes. The patterned substrates were then loaded into a horizontal flow low pressure (100 mbar) MOCVD system (Aixtron 200/4) and annealed at 750 °C for 10 min under a phosphine (PH_3) protective flow. The nanowires were grown at 730 °C for 20 min with trimethylindium (TMIn) and PH_3 at a flow rate of 6.1×10^{-6} and 4.9×10^{-4} mol/min, respectively. The total hydrogen (H_2) flow into the reactor was 15 L/min.

Optical characterization. A frequency-doubled solid-state laser (femtoTRAIN IC-Yb-2000) was used to pump individual nanowires (λ_{pump} = 522 nm, repetition rate 20.8 MHz, pulse length 300 fs) with a spot-size of 8.5 μm. Individual nanowires were excited through an aberration corrected 60x/0.70 numerical aperture, long working distance objective lens (Nikon CFI Plan Fluor) and the resulting emission was collected through the same objective. The collected light was spectrally filtered to remove the pump laser wavelength. Spectral measurements were made using a grating spectrometer (Acton, SpectraPro 2750) and a charge-coupled device (CCD) (Princeton Instruments, PIXIS). The focal plane of the lasing nanowires was imaged using the 0^{th} order of the grating and the spectrometer CCD. The back focal plane of the objective lens was imaged using a thin lens (f = 250 mm) and a separate CCD (Nikon DS-5Mc). For polarization analysis, a linear polarizer was inserted in the parallel beam path in the optical system, and the polarization axis of the polarizer was rotated to match the orientation of the nanowire. The low temperature experiments used He-cooled cryostat (Janis research) with a 0.019 inch thick chemically polished 0° sapphire window, through which the samples were optically excited and emission collected.

FIGURES

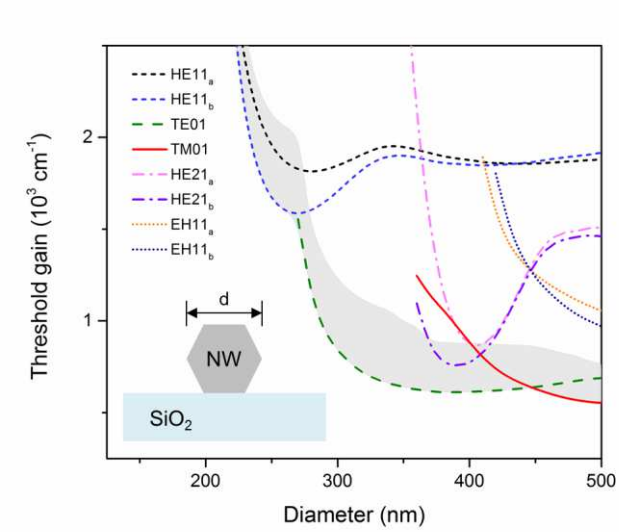

Figure 1. Threshold gain for single InP nanowire lying on a SiO_2 substrate. The threshold gain for different guided modes is modelled as a function of the nanowire diameter. The nanowire has a hexagonal cross-section and the diameter is defined as the widest length of the cross-section, as shown in the inset. The threshold gain is calculated using $\Gamma g_{th} \sim L^{-1} \ln(1/R)$, where R is the mode reflectance at the nanowire/air interface, Γ is the mode confinement factor and L is the cavity length. The mode reflectance and confinement factor for different modes was numerically evaluated using FDTD simulations (see Supporting Information) and L= 5 μm was used for these calculations. The region shaded in grey defines the values for which the difference in losses between the lowest-g_{th} modes is less than $1/\sqrt{p}$, where p is the number of cavity modes that can be coupled to within the emission spectrum. Modes with threshold gain values in this region are likely to lase.

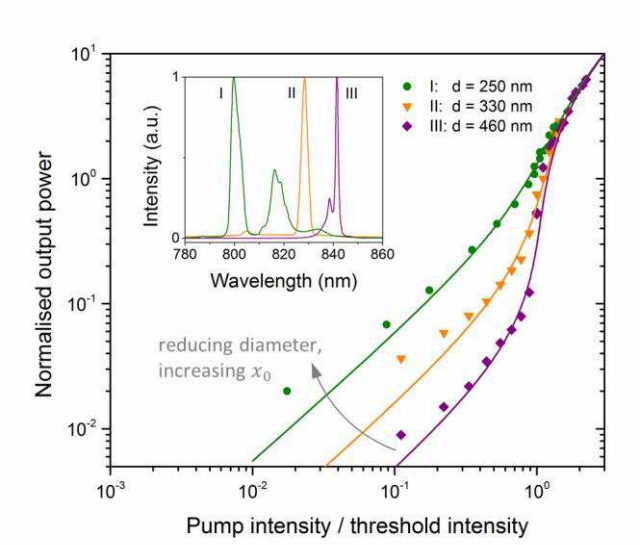

Figure 2. Lasing characteristics of three different optically pumped single InP nanowires. Lasing characteristics at low temperature (6 K) from three different InP nanowires of dimensions: (I) d=250 nm, L=3.9 μm, (II) d= 330 nm, L=2.8 μm, (III) d=460 nm, L=8.1 μm. The normalized output power versus pump intensity shows 'S' like behavior, which characterizes the transition from spontaneous emission to lasing via amplified spontaneous emission. The lines are calculated using Equation 23 in Ref 27, with values of the parameter x_0 = (I) 0.22, (II) 0.06, (III) 0.018, which provide a good fit to the experimental data. The 'S' like curve evolves from a sharp transition for large diameter nanowires to a soft transition for small diameter nanowires. The lasing spectra from these three nanowires, at pump intensity just above threshold ($P = 1.2*P_{th}$), is shown in the inset.

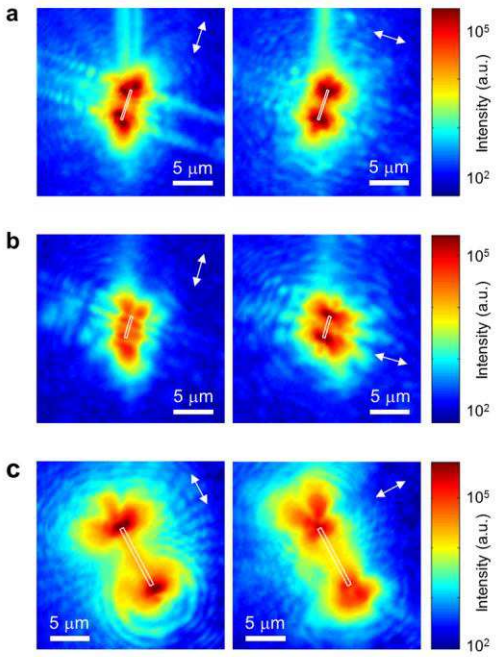

Figure 3. Polarization resolved focal plane images of three different InP nanowire lasers. The optically pumped InP nanowires were imaged above threshold, at pump intensity $P = 1.2*P_{th}$, with the pump laser filtered out. An analyzer was placed in front of the camera to resolve the polarization of the laser emission, both parallel and perpendicular to the nanowire axis. The white arrow at the top right hand corner of each image indicates the direction of the polarization axis of the analyzer. The lasing emission pattern from three nanowires, of diameters 250, 330 and 460 nm, is shown in **a-c**, respectively. The outline of the nanowire in each pattern is also shown. The polarization resolved images show distinct spatial patterns at positions corresponding to the nanowire end facets. The emission patterns are different for each of the three samples studied, and correspond well to far-field profiles of $HE11_b$, TE01 and TM01 modes, respectively (see Supporting Information). The color bar axes are on a log scale and the same color scale is used for each of the two different polarization images in **a-c**. The emission is predominantly polarized perpendicular to the nanowire in **b** and parallel to the nanowire in **c**.

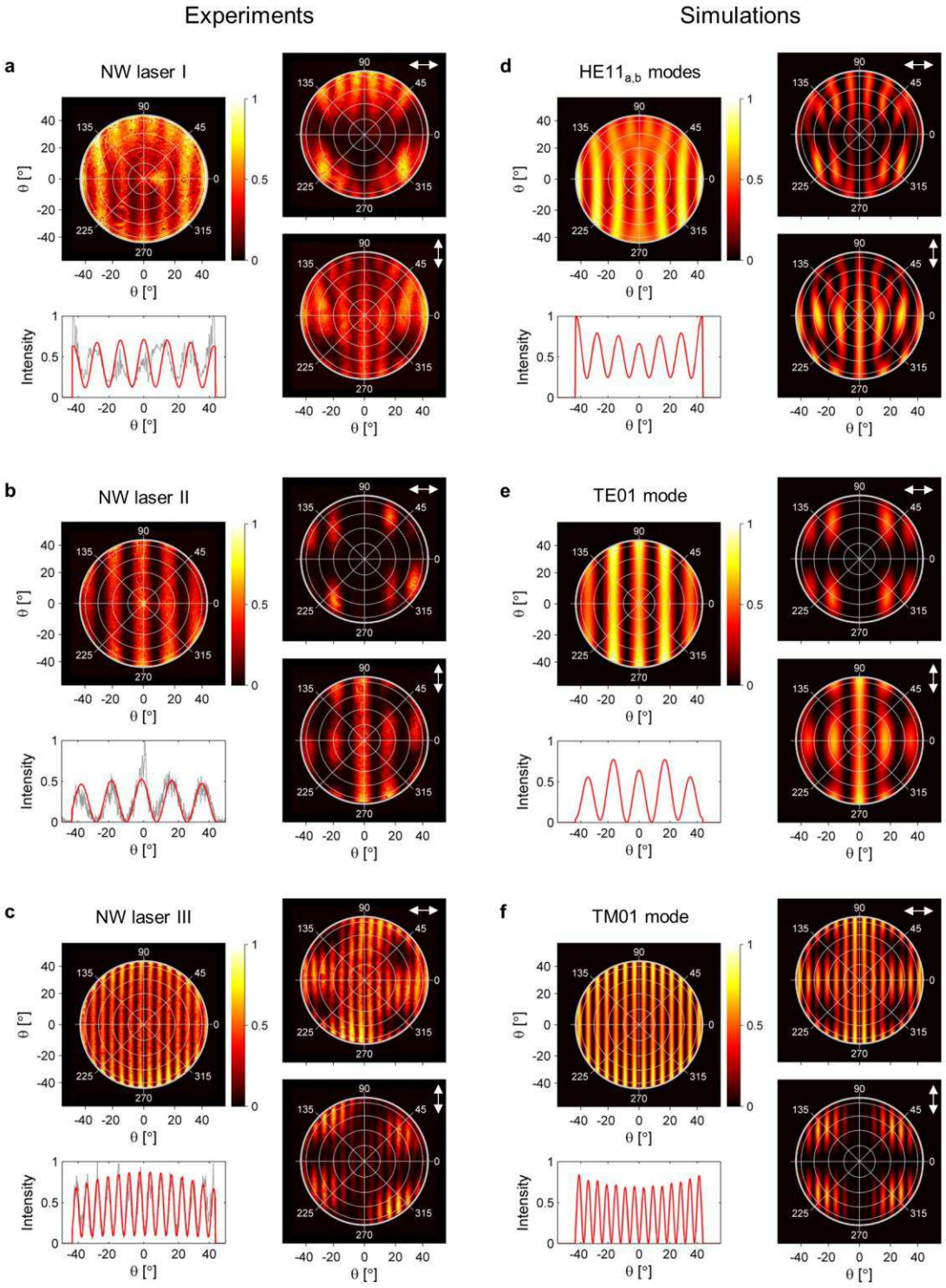

Figure 4. Mode characterization based on Fourier space imaging and numerical modelling of the far-field profiles. The experimentally obtained angle-resolved far-field emission patterns

from three InP nanowire lasers are shown in **a**-**c** and the simulated angle-resolved far-field patterns of $HE11_{(a,b)}$, TE01 and TM01 waveguide modes are shown in **d**-**f**, respectively. The top left hand image in each panel in **a**-**f** is the far-field intensity pattern and the right hand images in each panel are the polarization resolved far-field intensity patterns. The nanowire is orientated in the horizontal direction in each image, and the polarization is resolved parallel and perpendicular to the nanowire axis. The line plots in the bottom left of each panel shows the intensity modulation of the far-field pattern at ϕ=0° or 180°. In **a**-**c** the line plot of the experimental data is shown in grey and the intensity pattern calculated from an analytical model (see Supporting Information) is shown in red. In **e**-**f**, the line plot of the lasing mode far-field pattern obtained from FDTD simulations is shown. For the analytical calculations and FDTD simulations, the measured dimensions of the nanowire lasers I-III and their lasing wavelength were used (see Supporting Information).

ASSOCIATED CONTENT

Supporting Information. Additional information on the design of InP nanowire lasers, structural characterization of nanowires, measurement of nanowire laser dimensions, lasing spectra, simulations of the near-field and far-field mode profiles, analytical model to fit interference fringes across back focal plane, polarization analysis of the far-fields and corrections for the transmission through sapphire window. This material is available free of charge via the Internet at http://pubs.acs.org.

AUTHOR INFORMATION

Corresponding Author

*dhruv.saxena@anu.edu.au

Present Addresses

†Department of Chemistry and Biomolecular Sciences, Macquarie University, NSW 2109, Australia.

Author Contributions

D.S. and F.W. designed and conducted the experiments. Q.G. grew the nanowires. D.S. did the modelling and analysis in consultation with S.M.. H.T. and C.J. supervised the work. All authors contributed to the manuscript.

ACKNOWLEDGMENT

We acknowledge the Australian Research Council (ARC) for financial support, the National Computational Infrastructure (NCI) for providing the computational resources used for this work

and Australian Nano Fabrication Facility (ANFF) for technical support. We are grateful to Prof. Zhanghai Chen and Dr. Jian Lu for fruitful discussions on angle-resolved μ-PL experimental setup.

ABBREVIATIONS

PL, photoluminescence; SEM, scanning electron microscope; MOVPE, metal organic vapor phase epitaxy; CCD, charge-coupled device; FDTD, finite-difference time-domain; BFP, back focal plane; LED, light-emitting diode.

REFERENCES

1. Claudon, J.; Bleuse, J.; Malik, N. S.; Bazin, M.; Jaffrennou, P.; Gregersen, N.; Sauvan, C.; Lalanne, P.; Gerard, J.-M. *Nat Photon* **2010,** 4, (3), 174-177.
2. Reimer, M. E.; Bulgarini, G.; Akopian, N.; Hocevar, M.; Bavinck, M. B.; Verheijen, M. A.; Bakkers, E. P. A. M.; Kouwenhoven, L. P.; Zwiller, V. *Nat Commun* **2012,** 3, 737.
3. Johnson, J. C.; Choi, H.-J.; Knutsen, K. P.; Schaller, R. D.; Yang, P.; Saykally, R. J. *Nat Mater* **2002,** 1, (2), 106-110.
4. Duan, X.; Huang, Y.; Agarwal, R.; Lieber, C. M. *Nature* **2003,** 421, (6920), 241-245.
5. Zimmler, M. A.; Bao, J.; Capasso, F.; Muller, S.; Ronning, C. *Applied Physics Letters* **2008,** 93, (5), 051101-3.
6. Qian, F.; Li, Y.; Gradecak, S.; Park, H.-G.; Dong, Y.; Ding, Y.; Wang, Z. L.; Lieber, C. M. *Nat Mater* **2008,** 7, (9), 701-706.
7. Xiao, Y.; Meng, C.; Wang, P.; Ye, Y.; Yu, H.; Wang, S.; Gu, F.; Dai, L.; Tong, L. *Nano Letters* **2011,** 11, (3), 1122-1126.
8. Chen, R.; Tran, T.-T. D.; Ng, K. W.; Ko, W. S.; Chuang, L. C.; Sedgwick, F. G.; Chang-Hasnain, C. *Nat Photon* **2011,** 5, (3), 170-175.
9. Saxena, D.; Mokkapati, S.; Parkinson, P.; Jiang, N.; Gao, Q.; Tan, H. H.; Jagadish, C. *Nat Photon* **2013,** 7, (12), 963-968.
10. Gao, Q.; Saxena, D.; Wang, F.; Fu, L.; Mokkapati, S.; Guo, Y.; Li, L.; Wong-Leung, J.; Caroff, P.; Tan, H. H.; Jagadish, C. *Nano Letters* **2014,** 14, (9), 5206-5211.
11. Maslov, A. V.; Ning, C. Z. *IEEE J. Quantum Electron.* **2004,** 40, (10), 1389-1397.
12. Maslov, A. V.; Ning, C. Z. *Applied Physics Letters* **2003,** 83, (6), 1237-1239.
13. Ning, C. Z. *physica status solidi (b)* **2010,** 247, (4), 774-788.
14. Piccione, B.; Cho, C.-H.; van Vugt, L. K.; Agarwal, R. *Nat Nano* **2012,** 7, (10), 640-645.
15. Xiao, Y.; Meng, C.; Wu, X.; Tong, L. *Applied Physics Letters* **2011,** 99, (2), 023109-3.
16. Wu, X.; Xiao, Y.; Meng, C.; Zhang, X.; Yu, S.; Wang, Y.; Yang, C.; Guo, X.; Ning, C. Z.; Tong, L. *Nano Letters* **2013,** 13, (11), 5654-5659.
17. Maslov, A. V.; Ning, C. Z. *Optics Letters* **2004,** 29, (6), 572-574.
18. Mariano, A. Z.; Federico, C.; Sven, M.; Carsten, R. *Semicond. Sci. Technol.* **2010,** 25, (2), 024001.
19. Robert, R.; Daniel, P.; Arian, K.; Robert, B.; Sebastian, G.; Ulf, P.; Carsten, R. *Journal of Physics D: Applied Physics* **2014,** 47, (39), 394012.

20. Sun, L.; Ren, M.-L.; Liu, W.; Agarwal, R. *Nano Letters* **2014,** 14, (11), 6564-6571.
21. Grzela, G.; Paniagua-Domínguez, R.; Barten, T.; Fontana, Y.; Sánchez-Gil, J. A.; Gómez Rivas, J. *Nano Letters* **2012,** 12, (11), 5481-5486.
22. Bulgarini, G.; Reimer, M. E.; Bouwes Bavinck, M.; Jöns, K. D.; Dalacu, D.; Poole, P. J.; Bakkers, E. P. A. M.; Zwiller, V. *Nano Letters* **2014,** 14, (7), 4102-4106.
23. Bulgarini, G.; Dalacu, D.; Poole, P. J.; Lapointe, J.; Reimer, M. E.; Zwiller, V. *Applied Physics Letters* **2014,** 105, (19), 191113.
24. Intonti, F.; Riboli, F.; Caselli, N.; Abbarchi, M.; Vignolini, S.; Wiersma, D. S.; Vinattieri, A.; Gerace, D.; Balet, L.; Li, L. H.; Francardi, M.; Gerardino, A.; Fiore, A.; Gurioli, M. *Physical Review Letters* **2011,** 106, (14), 143901.
25. Coldren, L. A.; Corzine, S. W.; Masanovic, M. L., *Diode lasers and photonic integrated circuits*. Second ed.; Wiley: New Jersey, 2012.
26. Siegman, A. E., *Lasers*. University Science Books: Mill Valley, California, 1986.
27. Casperson, L. W. *J. Appl. Phys.* **1975,** 46, (12), 5194-5201.
28. Goodman, J. W., *Introduction to Fourier Optics*. 3rd ed.; Roberts & Company Publishers: Greenwood Village, 2005.
29. Hecht, E., *Optics*. 4th ed.; Addison Wesley: San Franscisco, 2002.
30. van Vugt, L. K.; Rühle, S.; Vanmaekelbergh, D. *Nano Letters* **2006,** 6, (12), 2707-2711.
31. Tchernycheva, M.; Messanvi, A.; de Luna Bugallo, A.; Jacopin, G.; Lavenus, P.; Rigutti, L.; Zhang, H.; Halioua, Y.; Julien, F. H.; Eymery, J.; Durand, C. *Nano Letters* **2014,** 14, (6), 3515-3520.
32. Chen, R.; Ng, K. W.; Ko, W. S.; Parekh, D.; Lu, F.; Tran, T.-T. D.; Li, K.; Chang-Hasnain, C. *Nat Commun* **2014,** 5.
33. Barrelet, C. J.; Bao, J.; Lončar, M.; Park, H.-G.; Capasso, F.; Lieber, C. M. *Nano Letters* **2006,** 6, (1), 11-15.
34. Nezhad, M. P.; Simic, A.; Bondarenko, O.; Slutsky, B.; Mizrahi, A.; Feng, L.; Lomakin, V.; Fainman, Y. *Nat Photon* **2010,** 4, (6), 395-399.
35. Heo, J. *Appl. Phys. Lett.* **2011,** 98, (2), 021110.
36. Wang, Z.; Tian, B.; Paladugu, M.; Pantouvaki, M.; Le Thomas, N.; Merckling, C.; Guo, W.; Dekoster, J.; Van Campenhout, J.; Absil, P.; Van Thourhout, D. *Nano Letters* **2013,** 13, (11), 5063-5069.

Table of Contents Graphic and Synopsis

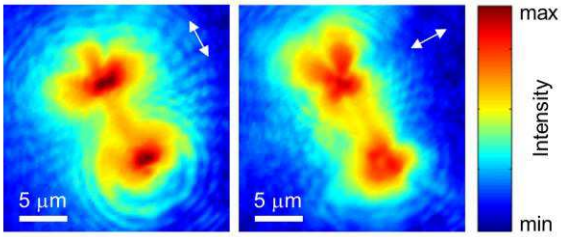

Far-field spatial profile of a nanowire laser resolved into two orthogonal polarizations: parallel and perpendicular to the nanowire axis.